LETTER
PLANETARY SCIENCES

Earth and Planetary Physics
4: 355–363, 2020
doi: 10.26464/epp2020055

Calibration of Mars Energetic Particle Analyzer (MEPA)

ShuWen Tang[1,3], Yi Wang[2], HongYun Zhao[1,3], Fang Fang[1], Yi Qian[1,3], YongJie Zhang[1,3], HaiBo Yang[1,3], CunHui Li[2], Qiang Fu[4], Jie Kong[1,3], XiangYu Hu[2], Hong Su[1,3], ZhiYu Sun[1,3]*, YuHong Yu[1,3]*, BaoMing Zhang[5], Yu Sun[1], and ZhiPeng Sun[1,3]

[1]Institute of Modern Physics, Chinese Academy of Sciences, Lanzhou 730000, China;

[2]Science and Technology on Vacuum Technology and Physics Laboratory, Lanzhou Institute of Physics, Lanzhou 730000, China;

[3]University of Chinese Academy of Sciences, Beijing 100049, China;

[4]Key Laboratory of Lunar and Deep Space Exploration, National Astronomical Observatories, Chinese Academy of Sciences, Beijing 100012, China;

[5]National Space Science Center, Chinese Academy of Sciences, Beijing 100190, China

Citation: Tang, S. W., Wang, Y., Zhao, H. Y., Fang, F., Qian, Y., Zhang, Y. J., Yang, H. B., Li, C. H., Fu, Q., Kong, J., Hu, X. Y., Su, H., Sun, Z. Y., Yu, Y. H., Zhang, B. M., Sun, Y., and Sun, Z. P. (2020). Calibration of Mars Energetic Particle Analyzer (MEPA). *Earth Planet. Phys.*, *4*(4), 355–363. http://doi.org/10.26464/epp2020055

Abstract: The first Mars exploration mission of China (Tianwen-1) is scheduled to be launched in 2020; a charged particle telescope, the Mars Energetic Particle Analyzer (MEPA), is carried as one of the payloads on the orbiter. The MEPA is designed to measure solar energetic particles (SEPs) and galactic cosmic rays (GCRs) in the near-Mars space and in the transfer orbit from Earth to Mars. Before the launch, the MEPA was calibrated in ground experiments with radioactive sources, electronic pulses, and accelerator beams. The calibration parameters, such as energy conversion constants, threshold values for the triggers, and particle identification criteria, were determined and have been stored for onboard use. The validity of the calibration parameters has been verified with radioactive sources and beams. The calibration results indicate that the MEPA can measure charged particles reliably, as designed, and that it can satisfy the requirements of the Tianwen-1 mission.

Keywords: Mars; Tianwen-1; MEPA; calibration

1. Introduction

As the second nearest and most similar planet to Earth, Mars is often the first choice for human exploration of other planets. Many Mars exploration missions have been performed since the 1960s (Portree, 2001; Saunders et al., 2004; Nielsen, 2004; Grotzinger et al., 2012). China's first Mars exploration mission, named Tianwen-1, will be launched in 2020. The probe is composed of an orbiter and a lander/rover (Ye PJ et al., 2017; Jiang XQ et al., 2018). As one of the payloads on the orbiter, the Mars Energetic Particle Analyzer (MEPA) is designed to measure and analyze the energetic charged particles in the Mars space and in the interplanetary space between Earth and Mars (Jia YZ et al., 2018); it will provide relevant information regarding radiation conditions in the Earth/Mars environment, data of obviously great importance for future human exploration of the Solar System.

Since Mars is quite distant from Earth and its environment is much harsher, the design of the MEPA has presented technical challenges significantly beyond those encountered in near-Earth explorations, and more detailed parameters have had to be determined in the calibrations. Typically, calibrations of a charged particle detector require the use of specific particles with well-known energies. The use of radioactive sources is the most convenient approach to such calibrations, but the particle species available on Earth are relatively few and their available energies are quite low compared to particles and energy levels that the probe can be expected to encounter. For calibrations involving more diverse species and higher energies, accelerator beams must be used. As for some unique characteristics that are hard to be measured directly, Monte–Carlo simulations are often used for these auxiliary calibrations (Golovko et al., 2008; Megna, 2009; Galford, 2017).

In this paper, we describe the detailed calibration of the MEPA in ground experiments with radioactive sources, accelerator beams, and Monte–Carlo simulations. The calibrations were carried out mainly as follows: First and most important were the energy calibrations, namely, to determine the relationship between the recorded ADC amplitudes and the deposited energies being recorded. In addition, the energy range and linearity of the electronics have been obtained. Besides, the trigger threshold settings and onboard event selection criteria were investigated. Finally, we report that the calibration parameters have been experimentally verified to be valid.

Correspondence to: Z. Y. Sun, sunzhy@impcas.ac.cn
Y. H. Yu, yuyuhong@impcas.ac.cn
Received 25 MAY 2020; Accepted 16 JUN 2020.
Accepted article online 20 JUL 2020.

2. Instrument Description

The MEPA instrument shown in Figure 1 consists of a sensor head and an electronics box; specifications are listed in Table 1. In order to detect diverse species of charged particles in a very wide energy range, as required with a single detector, the MEPA sensor head is designed as a compound ΔE–E telescope system, which includes a thin silicon detector (SD1), a thick silicon detector (SD2), and an inorganic thallium-doped cesium iodide scintillator detector (CsI). SD1 is Φ8 mm in diameter and 15 μm thick (MSD008 from Micron Semiconductor Ltd); SD2 is Φ26 mm by 300 μm thick (MSD026 from Micron Semiconductor Ltd). The CsI detector, manufactured in the Institute of Modern Physics, Chinese Academy of Sciences (IMPCAS), Lanzhou, China, is in the shape of a truncated hexagonal pyramid with a height of 32.5 mm. For the detection of light and fast charged particles with high penetrating power, SD2 will act as a ΔE detector and CsI will act as an E detector. On the contrary, for the detection of heavy and slow charged particles with low penetrating power, SD1 will act as a ΔE detector and SD2 will act as an E detector. The telescope system opens a 60° field of view (FOV) to accept charged particles. Meanwhile, in order to eliminate the effect of the particles coming from outside of the FOV, two plastic scintillator detectors are used to surround the telescope system as anti-coincidence detectors (ACD, EJ-200 from ELJEN Technology Ltd). The schematic of the MEPA sensor head is shown in Figure 2.

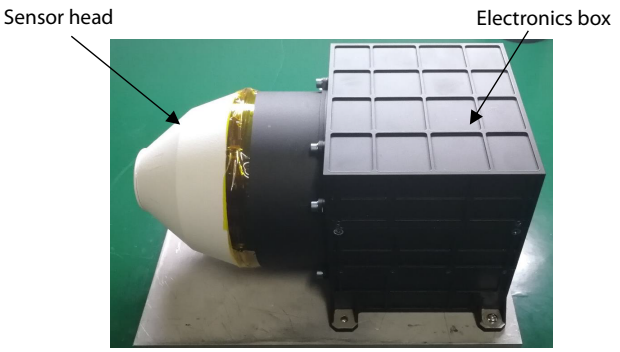

Figure 1. Photograph of the MEPA instrument.

Table 1. Specifications for MEPA.

Instrument Parameters	Characteristics
Particle species	Electrons, protons, heavy ions ($2 \le Z \le 26$)
Energy range	Electrons: 0.1–12 MeV; Protons: 2–100 MeV; Heavy ions: 25–300 MeV
Energy resolution	<15%
Flux range	0–10^5 $cm^{-2}s^{-1}$
Field of view	60°
Time resolution	4 s
Mass	≤ 3 kg
Power	<10 W
Volume	270mm × 180mm × 148mm
Data rate	≤ 1.3 kbps

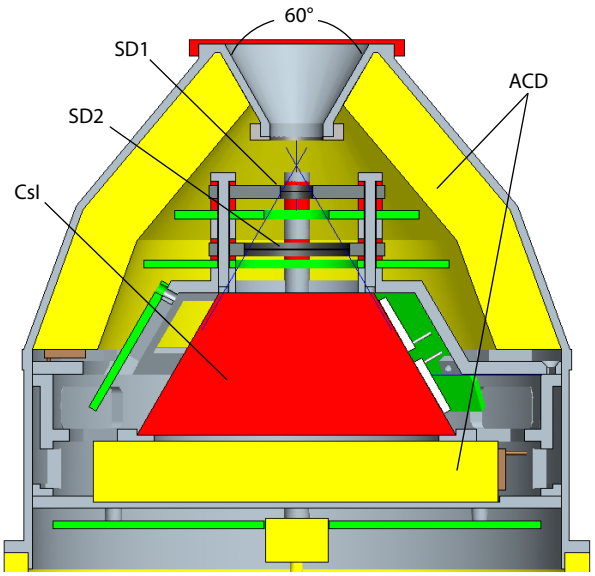

Figure 2. Schematic of the MEPA sensor head.

Charged particles entering the MEPA FOV will generate analog signals in silicon detectors and produce scintillation light in the CsI detector. Two sets of photoelectronic devices, each of which is comprised of a silicon photodiode (SiPD) and a silicon photomultiplier (SiPM), are glued on two opposite side faces of the CsI detector to collect the scintillation light. Analog signals from the silicon detectors or the SiPDs and SiPMs will be sent to the nearby FEE boards (green parts in Figure 2) inside the sensor head, where the signals will be pre-amplified and then sent to the electronic box. In order to maintain high resolution throughout a large energy range, the signals are split first and then sent to the channels in different gains to be amplified and shaped. According to the range of simulated energy loss in each individual detector, the output signal after FEE from SD1 is split into two different gain channels, one named SD1H and the other SD1L, corresponding to high gain and low gain, respectively; that from SD2 is split into three different gain channels, named SD2H, SD2M and SD2L. H, M, and L indicate high, medium, and low gain, respectively. Each SiPD signal is split into two gain channels, PD1H, PD1L, PD2H, and PD2L. The SiPM signals are not split, since they are used only for detecting quite small energy losses for the high gain of the SiPM device itself. Thus, there are 11 output signals in total for the MEPA telescope, each of which is fed to an individual channel of an ASIC chip, VA160, developed by IDEAS Inc. (Norway) (IDEAS, 2020). A 14-bit ADC and a field-programmable gated array (FPGA, A3PE3000L-1FG484M) are also included in the electronic box for processing the output signals from the VA160.

As the data transfer rate for the MEPA is very limited (≤ 1.3 kbps), it is not possible to transfer all the raw data to the payload controller in real time. The MEPA must perform analysis onboard for particle identification (PID) and total energy calculation. The main composition of the charged particle flux will be light particles, such as protons, helium, and electrons; heavy ions will account for

as little as 1% (Reedy and Howe, 1999; O'Neill, 2010). However, an onboard calculation algorithm for heavy ions would be most complicated, and beyond the computing power of the FPGA because of the quenching effect in the CsI detector. The MEPA will process data in different ways according to the particle types — for light particles with high flux ($Z \leq 2$) and heavy ions with low flux ($Z > 2$). The particle type is preliminarily identified by trigger levels, as follows: The MEPA is designed to have four trigger levels. Trigger level 1 (L1) is generated from the SD1 detector; trigger levels 2, 3, and 4 (L2, L3, L4) are generated from the high, medium, and low thresholds of SD2, respectively. The thresholds of L1 and L2 are carefully configured to be sufficiently high that no light particle can generate an effective trigger signal. As a result, if a trigger signal does originate from L1 or L2, the particle is reliably identified as a heavy ion. If a trigger signal originates from neither L1 nor L2, the particle is identified as a light particle. The MEPA analyzes raw data onboard only from the three species of light particles, calculating for each the total energy and the PID with the associated value of $\Delta E{\cdot}E$. Eventually, for every four seconds of the light particle flux, only the PID result and the histogram of the energy spectrum are transferred back for each light species; this compression greatly reduces the required data transfer rate. For the heavy ions, the calculation algorithm is quite complicated and thus impractical to perform onboard; fortunately, the very low flux of heavy ions allows the raw data to be transferred back for analysis on Earth.

In orbit, the MEPA has two operational modes. One is the observation mode, the other is the calibration mode. The observation mode is the normal mode for detecting charged particles; the calibration mode is a functional check mode for monitoring the electronic system.

3. Calibration and Performance

The MEPA measures the energy of a charged particle by processing correlated detection data from the silicon detectors and the CsI detector. The deposited energy is recorded in a 14-bit ADC for every channel. The strategy of the calibration is mainly to find the energy loss response curves (ELRC), namely the relationship between the deposited energy and the value recorded in the related ADC channel, for all 11 detector channels. Therefore, extensive calibration activities have to be done to ensure that all different gain channels are covered.

3.1 Calibration of Individual Detectors

Before assembly of the whole sensor head, the individual detectors of the MEPA were calibrated in the laboratory, using a wide range of radioactive sources and cosmic rays. In order to reduce the negative effects of air, all of these preliminary calibrations were performed in a vacuum.

First, the silicon detector SD2 was calibrated with a ^{207}Bi source, which emits monoenergetic electrons with energies of 481.7, 565.8, 975.7 and 1047.8 keV. The ^{207}Bi source was placed tightly close to the detector so as to enhance the possibility that energetic electrons deposit their full energy into the SD2. The resulting energy spectrum registered in the high gain channel of SD2 is shown in Figure 3a. An alpha source with three components of ^{239}Pu, ^{241}Am and ^{243}Cm (α particle energies: 5156, 5485 and 5784 keV) was also used for calibration. The energy spectrum obtained from the alpha source in the detector's medium gain channel is shown in Figure 3b.

The alpha source was used also to calibrate SD1. Since SD1 is very thin, the incoming α particles are fully stopped in SD1 only when coming into the detector at very large angles. Figure 4a shows the obtained energy spectrum in the high gain channel of SD1; the pedestal, penetrating events, and full-energy peak are all indicated. Considering that the vertical incoming particles have lost the least energy, the low edge of penetrating events could be used for calibration, together with the full-energy peak and the pedestal. The SD1 and SD2 were combined and calibrated as a telescope, again using the alpha source; results are shown in Figure 4b. All of the alpha particles penetrate SD1 and are stopped in SD2, so the deposited energy in SD1 plus the deposited energy in SD2 equals the total energy of all incident alpha particles; scatter points in Figure 4b show three separated lines.

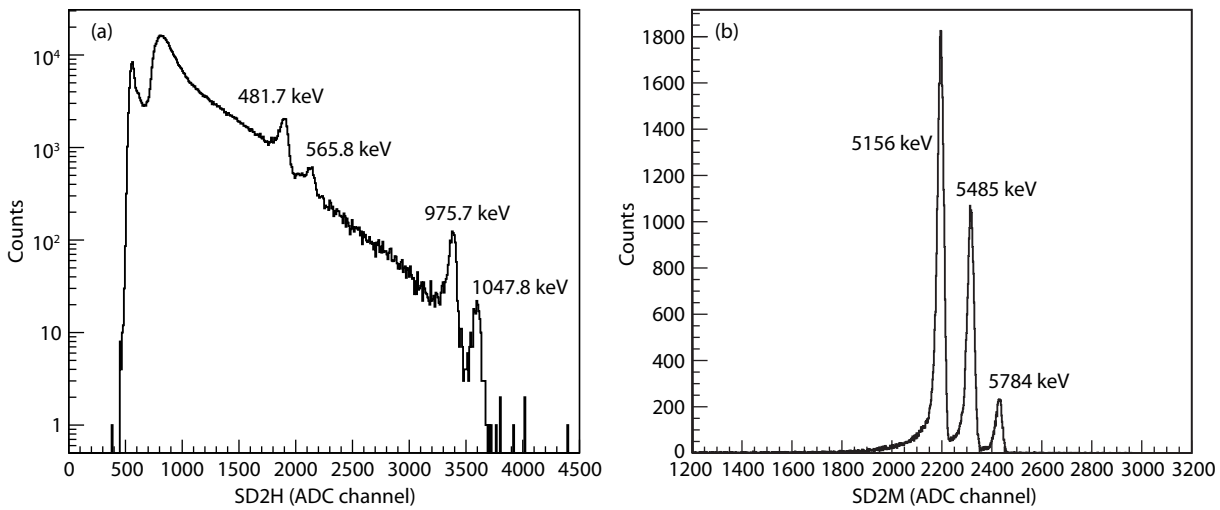

Figure 3. (a) Calibration of the SD2 with a ^{207}Bi source. (b) Calibration of the SD2 with an alpha source.

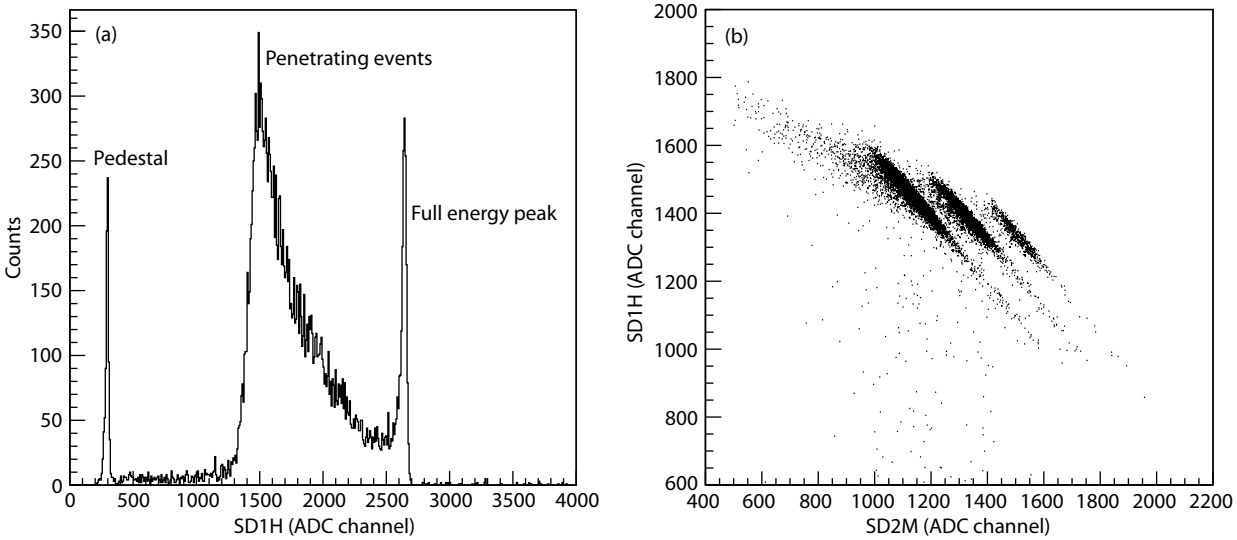

Figure 4. Calibration of SD1 detector with an alpha source. (a) The ADC response in the SD1H channel. (b) The correlative ADC responses in SD1H and SD2M; the three distinct lines represent the three different alpha particle energies.

As a result, after the calibration of SD2, SD1 could be calibrated by the relationship of deposited energies in SD1 and SD2.

The CsI detector was calibrated with γ-ray sources such as ^{137}Cs, ^{22}Na, and ^{60}Co. Since the energies of these laboratory radioactive sources are rather low, only the high gain channels could be calibrated; the medium and low gain channels, corresponding to higher energy ranges, would be done in the later beam calibrations.

As the ACD is used only for generating trigger signals, the amplitude information is not recorded. The most important function of the ACD is its detection efficiency. The ACD calibration is performed with ground cosmic rays. A dedicated setup was built for the calibration, consisting of (i) two large area scintillator detectors (S1 and S2) placed at the top and the bottom as the trigger detectors, and (ii) three position-sensitive detectors (PSD) installed between the scintillation detectors to determine the trajectories. The two parts of the ACD are placed in between the PSDs. Figure 5a shows a photograph of the ACD calibration setup; Figure 5b presents the schematic of the ACD calibration with cosmic rays. The detection efficiency of the ACD was calculated as $\eta = N/N_t$, where N_t corresponds to the total number of cosmic rays physically passed through the volume of the ACD, and N corresponds to the valid number of cosmic rays counted by the ACD. The threshold of the ACD has been carefully investigated with cosmic rays; the measured detection efficiencies for the top part and the bottom part of the ACD are both calculated as 99.9%.

3.2 Electronic Calibration

An electronic calibration system has been designed in the MEPA. It has a pulse generator associated with all 11 of the amplitude measurement channels. The reference voltage of the pulser is generated by a 12-bit DAC with a range from 0 to 2.5 V. During the calibration, the trigger signals were provided by the FPGA; all the triggers generated from real charge particles were shielded. For every channel, a series of pulses with given heights were generated and sent to the FEE. Then calibration signals went through

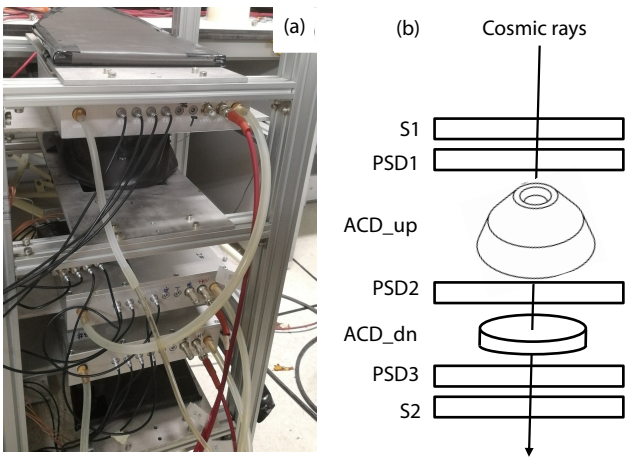

Figure 5. (a) Photograph of the ACD calibration setup; (b) Schematic of the calibration of ACD with cosmic rays.

the same circuits with the actual detector signals. An example of the electronic calibration in the SD1H channel is shown in Figure 6. Figure 6a presents pedestal information and the ADC response to every pulser signal. The linearity was analyzed for each channel (Figure 6b); the integral nonlinearity (INL) was found to be not more than 2%. Most important, the relationships between different gain channels for any individual detector were obtained (Figure 6c), which made it possible to calibrate the low gain channels with data from high gain channels obtained from radioactive source calibrations. Besides, the energy range for each channel could also be estimated according to the electronic calibrations. First, the calibration constants for every single channel were obtained from radioactive source calibrations and the electronic calibrations, and then they were updated and finalized after the beam calibrations.

The electronic calibration mode was used throughout the preflight testing period to monitor the functionality and stability of the electronic system; it can also provide the basis for in-flight

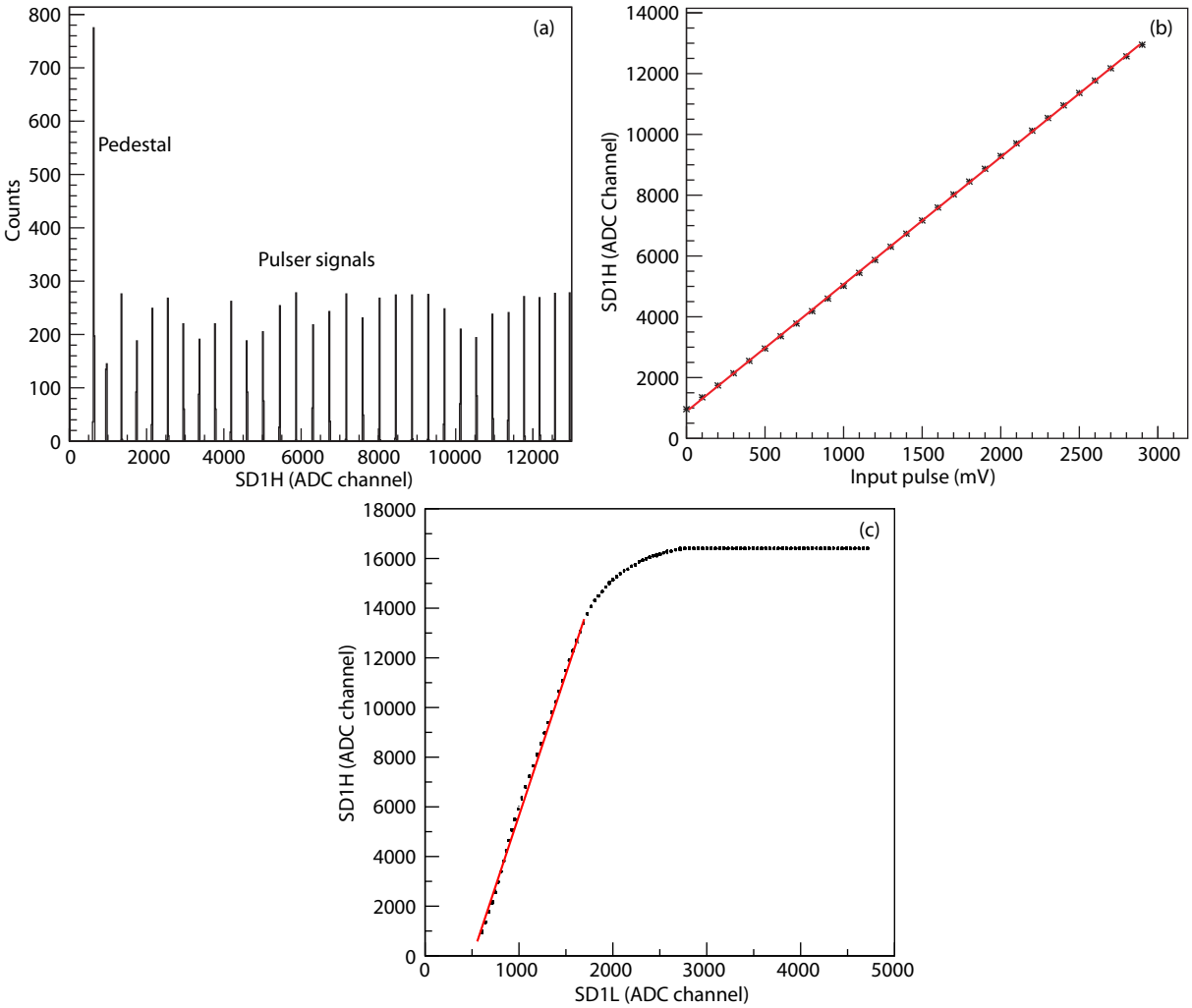

Figure 6. Electronic calibration of the SD1H channel. (a) Pedestal and ADC response to the pulser signals of different amplitudes; (b) The linearity response of the SD1H channel to input pulses; (c) The relationship between SD1H and SD1L.

electronic calibrations.

3.3 Instrument Calibration

3.3.1 Energy calibration

Since the radioactive source calibrations described in Section 3.1 were based on only a few species of particles of relatively low energy, additional accelerator calibrations were necessary and were performed after assembly of the MEPA. The completed instrument was calibrated at IMP in Lanzhou, China, where the accelerator HIRFL-RIBLL (Sun Z et al., 2003; Zhan WL et al., 2008) could provide many kinds of high energy charged particles. The accelerator calibration activities for the MEPA are listed in Table 2. Proton beams and ^{4}He beams of several different energies were used for calibration of the high and medium gain channels; ^{12}C and ^{22}Ne beams were used to bombard a beryllium target to produce a wide range of heavy ion fragments for calibration of the medium and low gain channels.

As a ΔE–E telescope, the MEPA identifies charged particles using a standard ΔE–E PID technique (Le Neindre et al., 2002). If a particle of charge Z and mass A has kinetic energy E and energy loss ΔE in the silicon detector, then it will obey the following equation:

$$\Delta E \times E \propto AZ^2 \quad (1)$$

The plot of ΔE vs. E forms a hyperbola, and any particular nuclide

Table 2. Accelerator calibration activities for the MEPA.

Particle Type	Facility	Energy (MeV)	Targets
Proton	HIRFL (China)	10、20、30、40、50、60、70、80	–
^{4}He	HIRFL (China)	35、80、120、150、200、250、300	–
^{12}C	HIRFL (China)	720	Be: 0.46 g/cm^2
^{22}Ne	HIRFL (China)	1353	Be: 0.74 g/cm^2

has its own hyperbola, which will appear separate from the hyperbolas of the other nuclides according to the value of AZ^2. We used ^{12}C and ^{22}Ne beams to bombard the target in order to produce a range of fragments on which to perform PID with the ΔE–E technique. Figure 7 shows an example of results of this technique with data from ^{22}Ne; the fragments from helium to fluorine can be identified clearly in the two-dimension spectrum between the low gain channel of SD2 and the low gain channel of SiPD in CsI. We were able to get the ADC values for all channels for every nuclide, and calculate the corresponding energy loss, using a software tool named LISE++ (Tarasov and Bazin, 2016).

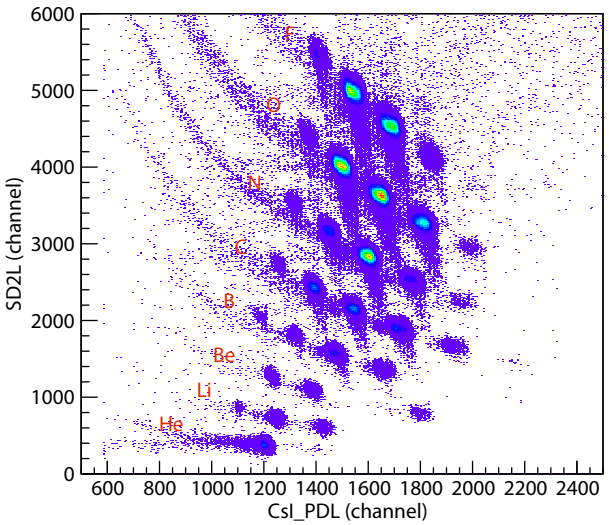

Figure 7. PID of fragments from a 1353 MeV ^{22}Ne beam bombarding a 0.74 g/cm^2 beryllium target.

The ELRC should be calculated with all the beam data and the radioactive source data. For silicon detectors, the yield of the electron-hole pairs is proportional to the deposited energy; therefore, the ELRC can be described very well with a simple linear function. As an example of the calibrations of SD1 and SD2, Figure 8 shows a linear fit to the experimental data for the medium gain channel of SD2.

However, the calibrations of the CsI detector were more complicated because of the quenching effect. The light output is not proportional to the energy loss but depends on the charge and mass of the charged particles. As mentioned above in Section 2, the MEPA processes data onboard in different ways depending on the type of particles (light particles or heavy ions) because of the limited data transfer rate and the complicated algorithm for heavy ions. So the calibration of the CsI was also separated by light particles (electrons, protons and helium) and heavy ions ($Z > 2$). For light particles, the linear relationship between light output and energy loss was used to reduce the amount of onboard calculation. Figure 9 shows the calibration of the CsI for light particles, presenting the low gain channel of an SiPD as an example. The result indicates that light particle experimental data could be satisfactorily fitted with a linear function, perhaps owing to the less significant quenching effect for light particles.

Since the quenching effect is no longer negligible as the charge goes higher, the calibrations for heavy ions had to be done with a nonlinear function. Birks proposed a differential light output dL/dx as the function of specific energy loss dE/dx (Birks, 1964):

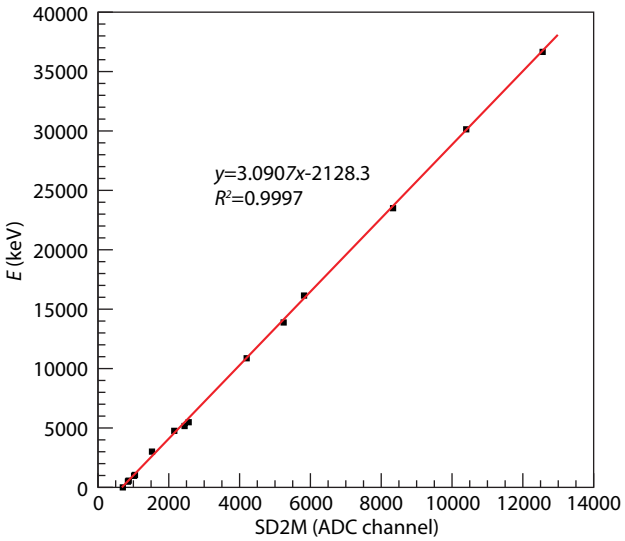

Figure 8. Calibration of silicon detectors.

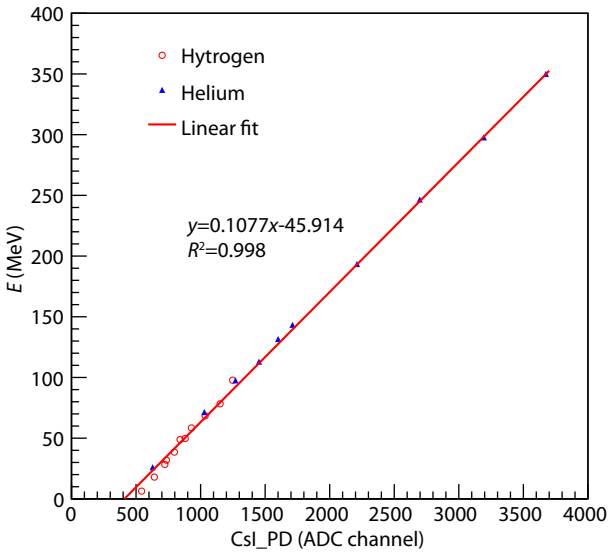

Figure 9. Calibration of the CsI with electrons, protons, and helium in the low gain channel of SiPD1; a linear relationship between light output and energy loss is used.

$$\frac{\mathrm{d}L}{\mathrm{d}x} = \frac{S}{(1 + kB\,(\mathrm{d}E/\mathrm{d}x))}, \tag{2}$$

where S is the scintillation efficiency, and kB is the so-called quenching factor referred to as the Birks constant. The light output can be obtained by an analytical integration of Equation (2) under the approximation of $\mathrm{d}E/\mathrm{d}x \propto AZ^2/E$ (Horn et al., 1992):

$$L\,(E, A, Z) = a_0 + a_1\left(E - a_2 AZ^2 \ln\left(\frac{E + a_2 AZ^2}{a_2 AZ^2}\right)\right), \tag{3}$$

where a_0, a_1, and a_2 are parameters obtained from a simultaneous fit of data. An example of the nonlinear calibration of the CsI for heavy ions is shown in Figure 10.

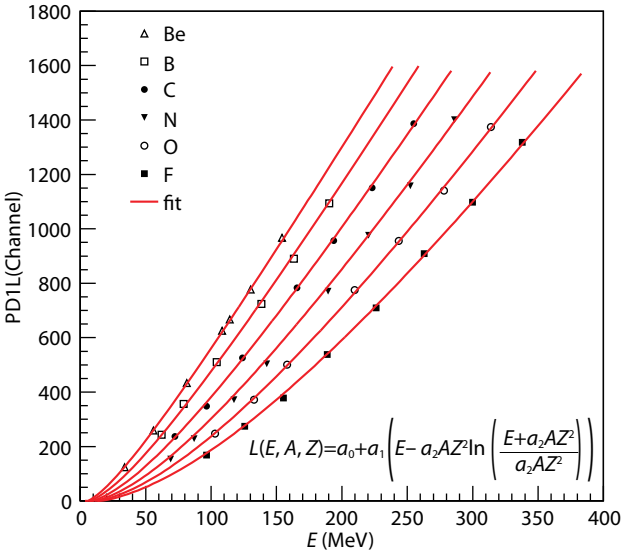

Figure 10. Calibration of CsI with heavy ions in the low gain channel of SiPD1, a nonlinear relationship between light output and energy loss has to be applied.

With the energy conversion constants for every channel, we can reconstruct the total energy for every incident particle, with $E_{sum} = E_{SD1} + E_{SD2} + E_{CsI} + E_{film}$. Here, E_{SD1}, E_{SD2}, and E_{CsI} correspond to the deposited energies in SD1, SD2 and CsI respectively, while E_{film} indicates the energy loss in the light barrier, a 2 μm-thick titanium film above SD1. E_{film} can be calculated with LISE++, after E_{SD1}, E_{SD2}, and E_{CsI} are determined; E_{film} is neglectable for most particles since the film is so thin. The reconstructed total energy for protons, helium, and heavy ions can be calculated with correlative beam data; the energy resolution obtained was less than 3% for all cases. Figure 11 shows an example of an energy spectrum reconstructed from the data of a 300 MeV helium beam; the energy resolution was calculated as 1.5%. Therefore, the energy resolution for heavy ions is better than 3% according to the calibration results. But for the light particles, since raw data are processed onboard and only histograms are transferred back, the energy resolution is determined primarily by the bin divisions of the histograms. For more detailed information, one can refer to the MEPA instrument paper.

3.3.2 Threshold calibration

The trigger thresholds are crucial since they are related to the preliminary identifications of particle type. The first step of the trigger threshold calibration was to find the relationship between the value of threshold DAC and the energy deposited in the corresponding silicon detector, which was done with the radioactive sources. Figure 12 shows an example of threshold calibration using ^{207}Bi for the low threshold of SD2 (L4); it indicates that the lower cut-off energy shifts when the value of the threshold DAC changes. We have obtained a series of correlative thresholds and cut-off energies with a ^{207}Bi source and an alpha source, fitted

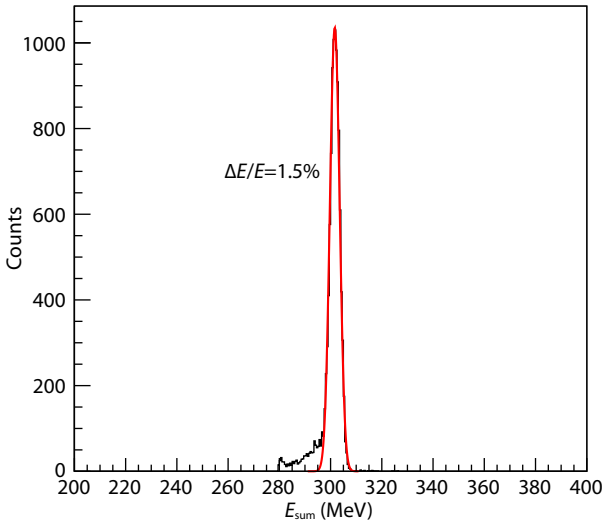

Figure 11. The total energy of a helium beam reconstructed from E_{SD1}, E_{SD2}, and E_{CsI}.

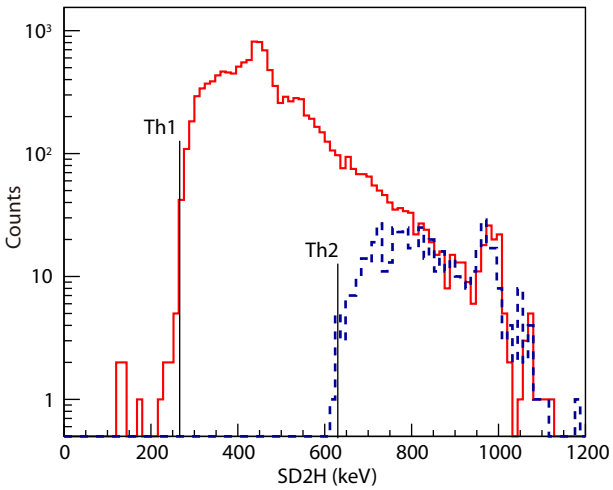

Figure 12. Calibration of the low threshold of SD2 with a ^{207}Bi source. The lower cut-off energy shifts with the threshold value.

them with a straight line, and thus found the relationship. The second step was to determine an appropriate threshold parameter for the onboard PID, which was done with Monte–Carlo simulations. The interactions of the MEPA with charged particles, from electron to Fe, were simulated with Geant4 — an open source Monte–Carlo software toolkit; it allowed the energy losses in SD1, SD2, and CsI to be obtained independently. The thresholds of L1 and L2 needed to be set higher than the maximum energy losses for electrons, protons, and helium in SD1 and SD2, respectively, so that only heavy ions could trigger L1 or L2. Therefore, a charged particle can be identified as a light particle or a heavy ion according to the trigger levels. The threshold of L4 could be determined by the noise level, which was obtained from the width of pedestals in the electronic calibration. After many tests in ground experiments, the noise was found to be approximatey 20 keV; the threshold of L4 was thus set at 50 keV to distinguish the signals from noises. The medium threshold of SD2 (L3) was set at ten times the L4 trigger threshold, so it is more reliable and has high-

er priority in trigger generation. As a result, the effective triggers are generated by the L3 trigger for energy deposited in SD2 greater than 500 keV, and generated by the L4 trigger for energy deposited in SD2 from 50–500 keV. This choice of use of the L3 trigger allows the MEPA to continue to work well even if the noise gets worse in flight.

After the preliminary particle type is identified by the trigger, raw data from heavy ions will be transferred back directly, while light particles will be analyzed further onboard. From the results of the Geant4 simulation, the energy losses in SD1, SD2, and CsI can be denoted as ΔE_1, ΔE_2, and ΔE_3, and SD2 plus CsI are always combined as the ΔE–E telescope. Therefore, $\Delta E = \Delta E_2$ and $E = \Delta E_2 + \Delta E_3$. Then the values of $\Delta E{\cdot}E$ for events not triggered by L1 and L2 are calculated and shown in Figure 13. There are a few heavy ions mixed in with the light particles; they can be separated easily by means of a threshold on the $\Delta E{\cdot}E$ value. However, electrons, protons, and helium cannot be distinguished simply by the $\Delta E{\cdot}E$ value alone, since some low energy particles are stopped in SD2. The particle species are identified clearly by considering additional energy loss in SD1. Eventually, all of the criteria for onboard PID are listed in Table 3.

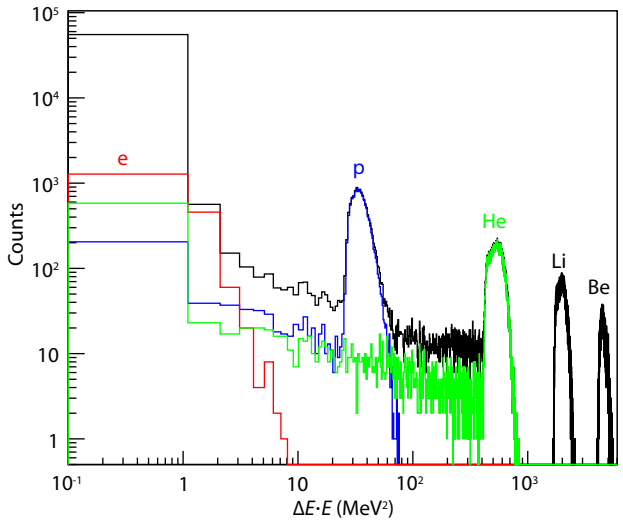

Figure 13. Spectrum of $\Delta E{\cdot}E$ from a simulation result.

Table 3. Onboard PID criteria for MEPA.

Particle Type	PID criteria (ΔE, E and ΔE_1 all in unit of MeV)
Electron	$\Delta E{\cdot}E \le 20$ && $\Delta E < 1$ && $\Delta E > 0.05$
Proton	$(20 < \Delta E{\cdot}E \le 150$ || $(\Delta E{\cdot}E \le 20$ && $\Delta E > 1))$ && $\Delta E_1 < 1$
Helium	$150 < \Delta E{\cdot}E \le 1200$ || $(\Delta E{\cdot}E \le 150$ && $\Delta E_1 \ge 1)$
Heavy ion	$\Delta E{\cdot}E > 1200$

3.4 Validation Test of the Calibration Parameters

After the calibration parameters were obtained, they were updated and stored in the FPGA. Then verification tests were performed to check the validation of the calibration parameters. First, the energy conversion constants were verified by proton and helium beams of known kinetic energies. The beam energies used for protons were 10, 20, 30, 40, 50, 60, 70, and 80 MeV; the helium beam energies were 35, 80, 120, 150, 200, 250, 300 and 350 MeV. The measured energies for every beam were calculated using the energy conversion constants. The results shown in Figure 14 agree very well with the incident energies.

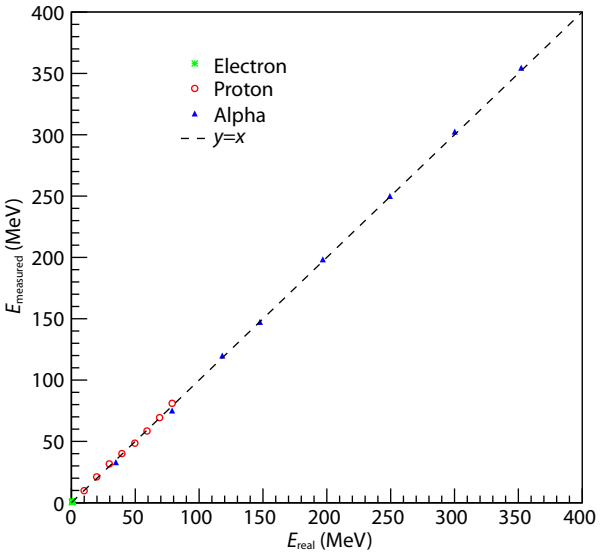

Figure 14. Verification of the energy parameters with proton beams and helium beams.

Incident particles are identified onboard by combining the trigger thresholds and the onboard PID criteria. During all of the light particle tests with electrons, protons, and helium, and for different energies, almost none of the events were triggered by L1 or L2, while ions with charge larger than four were all tagged by L1 or L2. Therefore, the trigger thresholds have been proven to yield reliable detection of particle type.

The energy loss in each individual detector for light particles is calculated onboard, and PID is performed according to the onboard PID criteria. The results tagged with the particle species, event by event, can be obtained. Figure 15 shows a ΔE vs. E spectrum obtained from the combination of a ^{207}Bi test, a proton beam test, and a helium beam test, where the color of the scatter points indicates the onboard PID results. It shows that the light particles were all properly identified as the correct particle species, verifying the validity of the onboard PID criteria.

4. Conclusions and Future Work

In summary, this paper describes in detail the ground calibrations of the MEPA instrument. The energy calibrations were performed using radioactive sources and accelerator beams, and the relationship between deposited energy and ADC response for each channel was obtained. The relationships have been shown to be simply linear for all of the silicon channels, but nonlinear for the CsI channels because of the quenching effect. However, as the quenching effect is quite slight for light particles such as electrons, protons, and helium, the energy relationships for such particles can be successfully approximated with linear functions, which has allowed the onboard algorithm to be simplified. The

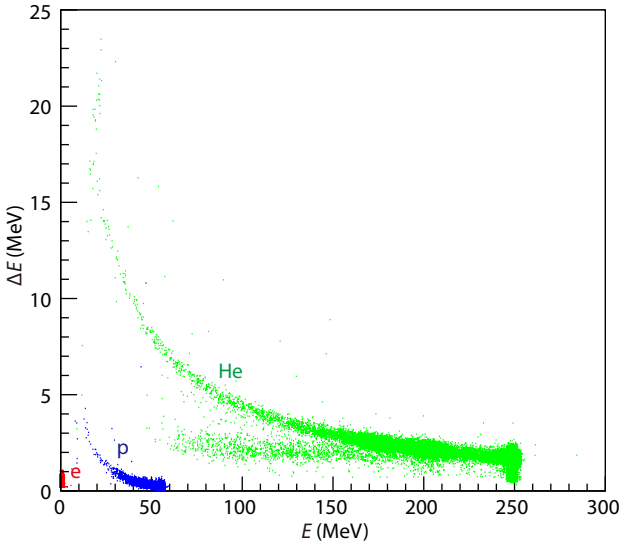

Figure 15. Verification of the PID criteria with a ^{207}Bi source and proton and helium beams.

nonlinear relationships necessary for analysis on Earth of raw data for heavy ions have also been determined. The efficiency of the ACD was calibrated using cosmic rays and determined to be approximately 99.9%. In addition, the pedestals and linearity for every channel were also calibrated electronically. The thresholds for all the triggers were established using radioactive sources, and the onboard criteria for particle identification were determined by a Monte–Carlo simulation. In the end, all of the calibration parameters have been demonstrated to be valid in the verification tests with radioactive sources and beams.

After the launch of Tianwen-1, MEPA will start its journey to Mars. More calibration work and data analysis should be done using the flight data.

Acknowledgments

This work is supported by the Engineering and Technological Research Project on Civil Aerospace Technologies of the CNSA. The authors thank the management and operators of the HIRFL-RIBLL facility for their efforts to make excellent beam time available.

References

Birks, J. B. (1964). *The Theory and Practice of Scintillation Counting* (pp. 465). Oxford: Pergamon Press. https://doi.org/10.1016/C2013-0-01791-4

Galford, J. E. (2017). A Monte Carlo modeling alternative for the API Gamma Ray Calibration Facility. *Appl. Radiat. Isotopes*, *122*, 47–56. https://doi.org/10.1016/j.apradiso.2017.01.004

Golovko, V. V., Iacob, V. E., and Hardy, J. C. (2008). The use of Geant4 for simulations of a plastic β-detector and its application to efficiency calibration. *Nucl. Instrum. Methods Phys. Res. Sect. A*, *594*(2), 266–272. https://doi.org/10.1016/j.nima.2008.06.025

Grotzinger, J. P., Crisp, J., Vasavada, A. R., Anderson, R. C., Baker, C. J., Barry, R., Blake, D. F., Conrad, P., Edgett, K. S., … Wiens, R. C. (2012). Mars science laboratory mission and science investigation. *Space Sci. Rev.*, *170*(1–4), 5–56. https://doi.org/10.1007/s11214-012-9892-2

Horn, D., Ball, G. C., Galindo-Uribarri, A., Hagberg, E., Walker, R. B., Laforest R., and Pouliot, J. (1992). The mass dependence of CsI(Tl) scintillation response to heavy ions. *Nucl. Instrum. Methods Phys. Res. Sect. A*, *320*(1–2), 273–276. https://doi.org/10.1016/0168-9002(92)90785-3

IDEAS. 2020. Integrated Detector Electronics AS. http://www.ideas.no/.

Jia, Y. Z., Fan, Y., and Zou, Y. L. (2018). Scientific objectives and payloads of Chinese first Mars exploration. *Chin. J. Space Sci.*, *38*(5), 650–655. https://doi.org/10.11728/cjss2018.05.650

Jiang, X. Q., Yang, B., and Li, S. (2018). Overview of China's 2020 Mars mission design and navigation. *Astrodynamics*, *2*(1), 1–11. https://doi.org/10.1007/s42064-017-0011-8

Le Neindre, N., Alderighi, M., Anzalone, A., Barnà, R., Bartolucci, M., Berceanu, I., Borderie, B., Bougault, R., Bruno, M., … Zipper, W. (2002). Mass and charge identification of fragments detected with the Chimera Silicon–CsI(Tl) telescopes. *Nucl. Instrum. Methods Phys. Res. Sect. A*, *490*(1–2), 251–262. https://doi.org/10.1016/S0168-9002(02)01008-2

Megna, R. (2009). Monte Carlo simulation studies of the timing calibration accuracy required by the NEMO underwater neutrino telescope. *Nucl. Instrum. Methods Phys. Res. Sect. A*, *602*(1), 80–83. https://doi.org/10.1016/j.nima.2008.12.008

Nielsen, E. (2004). Mars express and MARSIS. *Space Sci. Rev.*, *111*(1–2), 245–262. https://doi.org/10.1023/B:SPAC.0000032712.05204.5e

O'Neill, P. M. (2010). Badhwar-O'Neill 2010 galactic cosmic ray flux model—revised. *IEEE Trans. Nucl. Sci.*, *57*(6), 3148–3153. https://doi.org/10.1109/TNS.2010.2083688

Portree, D. S. F. (2001). Humans to Mars: fifty years of mission planning, 1950–2000. NASA SP-2001-4521.

Reedy, R. C., and Howe, S. D. (1999). The Martian radiation environment from orbit and on the surface. In *Workshop on Mars 2001: Integrated Science in Preparation for Sample Return and Human Exploration*. Houston: Lunar and Planetary Institute. https://hdl.handle.net/20.500.11753/896

Saunders, R. S., Arvidson, R. E., Badhwar, G. D., Boynton, W. V., Christensen, P. R., Cucinotta, F. A., Feldman, W. C., Gibbs, R. G., Kloss, Jr. C., … Zeitlin, C. J. (2004). 2001 Mars odyssey mission summary. *Space Sci. Rev.*, *110*(1–2), 1–36. https://doi.org/10.1023/B:SPAC.0000021006.84299.18

Sun, Z., Zhan, W. L., Guo, Z. Y., Xiao, G., and Li, J. X. (2003). RIBLL, the radioactive ion beam line in Lanzhou. *Nucl. Instrum. Methods Phys. Res. Sect. A*, *503*(3), 496–503. https://doi.org/10.1016/S0168-9002(03)01005-2

Tarasov, O. B., and Bazin, D. (2016). LISE^{++}: Exotic beam production with fragment separators and their design. *Nucl. Instrum. Methods Phys. Res. Sect. B*, *376*, 185–187. https://doi.org/10.1016/j.nimb.2016.03.021

Ye, P. J., Sun, Z. Z., Rao, W., and Meng L. Z. (2017). Mission overview and key technologies of the first Mars probe of China. *Sci. China Technol. Sci.*, *60*(5), 649–657. https://doi.org/10.1007/s11431-016-9035-5

Zhan, W. L., Xia, J. W., Zhao, H. W., Xiao, G. Q., Yuan, Y. J., Xu, H. S., Man, K. D., Yuan, P., Gao, D. Q., … HIRFL-CSR Group. (2008). HIRFL today. *Nucl. Phys. A*, *805*(1–4), 533c–540c. https://doi.org/10.1016/j.nuclphysa.2008.02.292